LANGMUIR

pubs.acs.org/Langmuir Article

Effect of Polymer Length on the Adsorption onto Aluminogermanate Imogolite Nanotubes

Giuseppe Cavallaro, Giuseppe Lazzara,* Frédéric Pignon, Leonardo Chiappisi, and Erwan Paineau*

Cite This: *Langmuir* 2021, 37, 9858–9864 Read Online

ACCESS | Metrics & More | Article Recommendations | Supporting Information

ABSTRACT: This study evidences the adsorption of model nonionic polymers onto aluminogermanate imogolite nanotubes, attractive porous nanofillers with potential molecular loading and release applications. We resolve the underlying mechanisms between nanotubes and polyethylene glycols with different molecular weights by means of nanoisothermal titration calorimetry. The analysis of the results provides a direct thermodynamic characterization, allowing us to propose a detailed description of the energetics involved in the formation of polymer/imogolite complexes. The affinity toward the nanotube surface is enthalpy-driven and strongly depends on the polymer chain length, which significantly affects the polymer configuration and the flow properties of the resulting complexes, probed by small-angle neutron scattering and rheology, respectively. These findings open new avenues for the rational design of these hybrid mixtures for advanced applications.

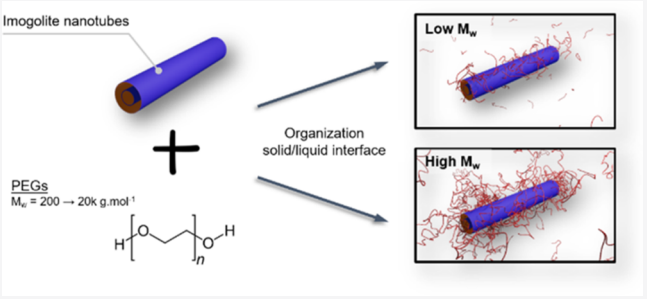

INTRODUCTION

An imogolite nanotube (INT) is an aluminosilicate clay mineral, naturally occurring and widespread in well-drained volcanic ash soils.[1] Unlike halloysite, another tubular clay mineral,[2] INTs can be readily synthesized through hydrothermal methods.[3,4] The structure of these nanotubes is rather unique. The external walls consist of gibbsite-like sheets $Al(OH)_3$, while the cavity interface is formed by isolated $(SiO_3)OH$ tetrahedron units connected upright to the octahedral vacancies by covalent bonding.[5] Silicon can be replaced by germanium allowing us to increase the diameter of the inner cavity from 1.5 to 3 nm for single-walled INTs.[6,7] Furthermore, modifications of the synthesis conditions offer a convenient way for designing innovative INTs with well-defined morphologies (single- or double-walled structures),[8] modular interfaces (e.g., hydrophilic or hydrophobic cavities),[9−11] and high colloidal stability in aqueous media.[12−14] All these properties have led in recent years to a renewed interest in synthetic imogolite-type nanotubes as promising nanoreactors notably for molecular confinement[15−18] or photocatalytic applications.[19−23]

INT offers similar characteristics to carbon nanotubes (CNTs) in terms of rigidity, sizes, and aspect ratios while retaining transparency and self-organization under highly dilute conditions.[24,25] Although they display larger band gaps than CNTs,[26] they are cheaper to produce with monodisperse diameters without further sorting techniques. Consequently, INTs represent as interesting alternatives of the CNTs in numerous applications including the fabrication of polymer/filler nanocomposites with multifunctional characteristics. Within this, imogolite was successfully employed with various polymers as a reinforced filler for functional nanocomposites with enhanced mechanical, optical, or electrical properties, including self-healing capability.[27−34] An interesting advantage of INTs is the high density of hydroxyl groups on the outer surface (~18 OH/nm^2). It should promote different possibilities of polymer adsorption[35] or change in conformation as shown recently by nuclear magnetic resonance.[36,37] To date, however, the underlying mechanisms remain largely unexplored.

One of the most used techniques to probe the polymer−nanoclay interaction mechanism is isothermal titration calorimetry (ITC), which allows the experimentalist to determine the thermodynamic parameters for the adsorption phenomenon through direct measurements. It allowed clarifying the interactions in terms of hydrophobic/electrostatic forces and polymer degree of freedom through the evaluation of the entropic contribution.[38,39] Moreover, the determination of the adsorption isotherm and the maximum amount of polymers adsorbed per mass of nanoclay in comparison with the polymer gyration radius and geometric features of the nanoparticle provided an indirect representation

Received: June 9, 2021
Revised: July 22, 2021
Published: August 9, 2021

https://doi.org/10.1021/acs.langmuir.1c01549
Langmuir 2021, 37, 9858−9864

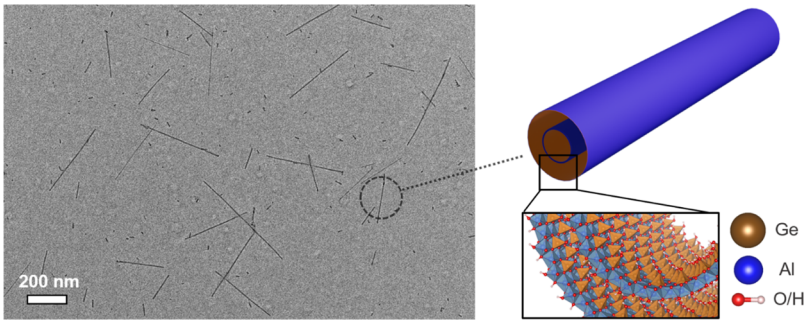

Figure 1. Representative transmission electron microscopy image of aluminogermanate double-walled INTs (Ge−DWINTs). The sketch in the right illustrates the atomic structure of a Ge-DWINT with the curved $Al(OH)_3$ sheet (in blue) and isolated $(GeO_3)OH$ units (in orange). Oxygen and hydrogen atoms are represented in red and white, respectively.

on the polymer conformation at the interface.[40] It should be noted that isothermal calorimetry is the only correct approach to determine the enthalpy change of a reaction if the stoichiometry may change with temperature as, in the latter case, the well-known van't Hoff approach cannot be used.[41]

Here, we investigated the adsorption of nonionic polymers with variable molecular weights on the outer surface of anisometric double-walled germanium-based imogolite (Ge−DWINTs) with an outer diameter of 4.5 nm and an average length of around 100 nm (Figure 1).[14] Polyethylene glycols (PEGs) with variable molecular weights are selected as model hydrosoluble nonionic polymers that are frequently added with clay minerals.[42−44] We proposed the first detailed description on the energetics involved in the formation of polymer/imogolite complexes by combining ITC measurements with small-angle neutron scattering (SANS) and rheological experiments. The determination of thermodynamic parameters allowed predicting the fraction of the polymer adsorbed onto the nanotube surface. The adsorption mechanism is dependent on the PEG chain length, modifying the conformation and the flow properties of the resulting mixtures.

EXPERIMENTAL SECTION

Materials. PEGs with various average molecular weights (M_w = 200, 400, 2k, 3k, and 20k g·mol^{-1}) were purchased from Sigma-Aldrich. Polymer solutions have been prepared by weight (±0.01 mg) and keeping under magnetic stirring overnight. Details on the synthesis and characterizations of Ge-DWINTs have been reported elsewhere.[45] After dialysis, the as-obtained Ge−DWINTs form stable colloidal dispersions (C = 10 g·L^{-1}), where the nanotubes are individually dispersed.[24] Mixtures of Ge−DWINTs with PEGs were prepared by adding the appropriate amount of the polymer at different polymer/imogolite mass ratios ($R_{P/INTs}$) while keeping the imogolite concentration constant.

Isothermal Titration Calorimetry. ITC experiments were performed by using the ultrasensitive nano-ITC200 calorimeter (MicroCal). An amount of approximately 40 μL of the water/polymer mixture was injected into the thermally equilibrated ITC cell (200 μL) containing the water/imogolite dispersion (concentration of 4.47 mg·L^{-1}). Each addition step was 0.49 μL. Volumes have been calibrated by the NaCl dilution experiment.[46] The concentration of the polymer solutions was ca. 5 g·L^{-1}. The cell was thermally equilibrated at 25.000 ± 0.005 °C. The calorimeter sensitivity is at least 2 nanoW. The raw data were corrected for the instrument time constant, and an appropriate baseline was subtracted.

Small-Angle Neutron Scattering. SANS measurements were carried out at Institut Laue-Langevin (ILL), Grenoble (France), using the instrument D11.[47] The experiments were conducted at two different configurations with the sample-to-detector (and collimation in parenthesis) distances of 2 m (5 m) and 8 m (8 m) using a wavelength λ of 6 Å and a full width at half-maximum of 10%. The scattering vector q was calculated as $4\pi\sin\theta 2\lambda$, θ being the scattering angle. The two-dimensional patterns were corrected for the detector efficiency using the scattering of a 1 mm H_2O sample and for the dark current signal. The contribution from the H_2O/D_2O solvent was subtracted, and finally, the patterns were radially averaged, the scattering being isotropic. Data reduction was performed using berSANS,[48] while SASfit 0.94.11 software was used for the analysis of SANS curves.[49] The experiments were performed by diluting the stack Ge−DWINT dispersion with D_2O, and the final solvent was H_2O/D_2O with a mass ratio of 1/10. The density (±1 × 10^{-6} g cm^{-3}) of the Ge−DWINT dispersion was determined by using a DSA 5000 M (Anton Paar) at 25 °C (±0.001 °C). The specific volume of the INTs was calculated as

$$V_{sp} = \left(\frac{1}{d}\right) - 10^3\frac{(d - d_0)}{wdd_0} \quad (1)$$

where d is the experimental density for Ge−DWINT dispersion at concentration w (expressed as g of Ge−DWINTs/kg of the solvent) and d_0 is the water density.

Rheology. Rheological measurements were performed using a controlled-stress rheometer (Discovery HR-3, TA Instruments) using a cone-plate geometry (60 mm in diameter and 1° in angle) and a solvent trap cover to prevent sample evaporation. Flow curves of PEGs/Ge−DWINTs ($R_{P/INTs}$ = 10) were measured under a controlled shear rate from 1 to 2200 s^{-1}.

RESULTS AND DISCUSSION

Thermodynamic Characterization of PEG/Ge-DWINT Dispersions. The thermodynamics of the polymer adsorption onto the aqueous dispersions of Ge−DWINTs was investigated by ITC through the stepwise injection method. The effects of dilution of the polymer and imogolite were measured and subtracted from the heats of titration to obtain the thermal effects of the polymer/imogolite interaction at each step. Based on the ITC data, we determined the cumulative variation of enthalpy (ΔH_{ic}) at variable polymer/imogolite mass ratios ($R_{P/INTs}$) for PEGs with different molecular weights (Figure 2). Details for the calculation of ΔH_{ic} are presented in the Supporting Information.

As for the other polymer/clay systems,[38,40] the ΔH_{ic} versus $R_{P/INTs}$ trends correspond to a single adsorption process that were successfully described by the Langmuir adsorption model (Figure 2), providing the enthalpy (ΔH_{ads}^0) and the equilibrium constant (K_{ads}) for the PEG adsorption onto imogolite surfaces. According to the K_{ads} and ΔH_{ads}^0 values, we estimated the standard free energy (ΔG_{ads}°) and the entropy (ΔS_{ads}°) for the adsorption process as

$$\Delta G_{ads}^\circ = -RT \ln K_{ads} \quad (2)$$

https://doi.org/10.1021/acs.langmuir.1c01549
Langmuir 2021, 37, 9858−9864

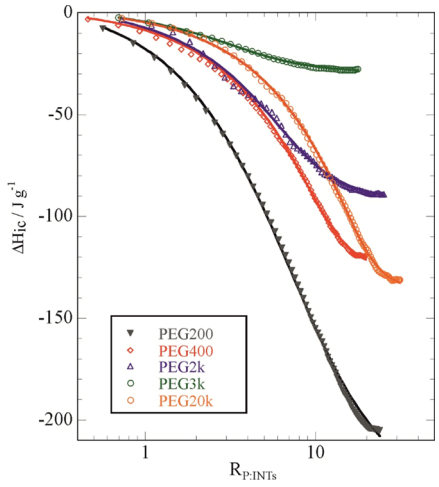

Figure 2. Isothermal titration data of Ge−DWINTs with PEGs of different molecular weights. Lines correspond to the best fits according to the Langmuir adsorption model.

$$T\Delta S^{\circ}_{ads} = \Delta H^{\circ}_{ads} - \Delta G^{\circ}_{ads} \quad (3)$$

In addition, the fitting of ITC data (Figure 2) allowed us to determine the PEG/INT stoichiometry (Z) at the saturation point. Namely, Z represents the maximum amount of PEG moles adsorbed per gram of INTs. The fitting analysis of the experimental ΔH_{ic} versus $R_{P/INTs}$ functions is detailed in the Supporting Information.

Table 1 collects the thermodynamic parameters and the stoichiometry values for the adsorption of PEGs with variable molecular weights onto imogolite.

As evidenced from Table 1, the polymer molecular weight affects both the thermodynamic parameters and the maximum mass of PEG adsorbed onto Ge−DWINTs. The equilibrium constant displays a monotonic evolution according to the PEG chain length, and it is related to different affinities. As shown for clay nanosheets, a limited affinity for the clay surface was observed for PEG with a low molecular weight (1000−4000 g·mol^{-1}), whereas higher values resulted in an increase of the adsorbed mass of the polymer in conjunction with a change of the polymer conformation.[50,51] The negative values of standard free energy indicate that PEG adsorption onto the Ge−DWINT surface is energetically favored. Both ΔG_{ads}° and ΔH_{ads}° decrease with the PEG molecular weight, which indicates an enthalpy-driven adsorption process for all the mixtures. Given that the enthalpy of adsorption per mole of the polymer is always negative, PEG/imogolite interactions are the dominant forces in the adsorption process, although the enthalpic contribution is much more relevant for polymers with a longer chain. As concerns ΔS_{ads}°, we determined positive values for all the PEGs used in this work (except for PEG20k). In general, the change in entropy is related to the following contrasting effects: (i) a loss of configuration freedom of the polymer in the adsorbed state, which induces a decrease of entropy ($\Delta S_{ads}^{\circ} < 0$) or (ii) a water release from the polymer ($\Delta S_{ads}^{\circ} > 0$). The positive entropy values highlight that dehydration from the adsorbed PEG represents the dominant entropic factor during the adsorption. On the other hand, $\Delta S_{ads}^{\circ} < 0$ was observed for the highest molecular weight, suggesting that the dehydration phenomenon is less relevant for this mixture.

The maximum amount of PEG molecules adsorbed onto the imogolite surface decreases sharply with the polymer molecular weight (Z values in Table 1), and therefore, the most hydrated structure is expected for PEG20k compared to that for the other polymers. Based on the thermodynamic parameters (Table 1), we can deduce the fraction of polymers adsorbed onto imogolite surfaces at variable $R_{P/INTs}$. Based on the fitting parameters of ITC curves (see details in the Supporting Information), we calculated the fraction of the polymer adsorbed onto imogolite as a function of $R_{P/INTs}$ for PEG2k/INT and PEG20k/INT complexes (Figure 3).

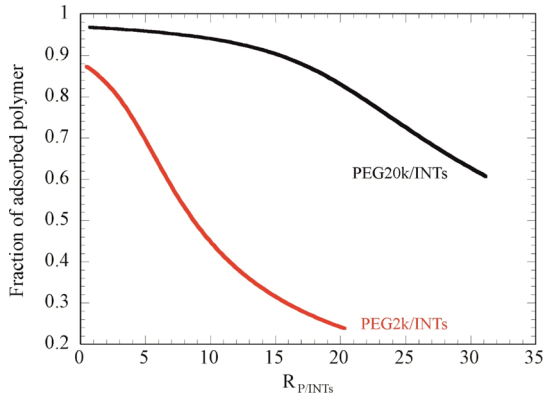

Figure 3. Calculated fraction of the polymer adsorbed onto Ge−DWINTs at variable $R_{P/INTs}$ for Ge−DWINT complexes with PEG2k (red) and PEG20k (black).

Within the investigated polymer/Ge−DWINT range, we estimated a larger adsorbed fraction for PEG with the longest chain. For example, for $R_{P/INTs}$ = 10, the fractions of the polymer adsorbed onto Ge−DWINTs are ca. 0.4 and 0.95 for PEG2k and PEG20k, respectively. The different adsorption profiles are the result of the equilibrium constant, weighted by the maximum possible amount of polymers that can be allocated at the solid/liquid interface. In other words, there is more place for small polymers (expressed in total mass) but less tendency to fill that space as evidenced by the equilibrium constants.

Table 1. Investigated PEG with Various Molecular Weights and the Corresponding Adsorption Parameters Deduced from ITC Measurements Performed at 298 K

polymer	molecular weight (g·mol^{-1})	K_{ads}(dm^{3}mol^{-1})	Z^a (mmol$_P$ g$_{INTs}^{-1}$)	ΔH_{ads}^0 (kJ mol^{-1})	ΔG_{ads}^0 (kJ mol^{-1})	ΔS_{ads}^0 (kJ mol^{-1} K^{-1})
PEG200	200	$(9.5 \pm 1.7) \times 10^4$	37 ± 2	−2.15 ± 0.17	−28.8 ± 0.5	0.088 ±0.007
PEG400	400	$(1.6 \pm 0.4) \times 10^6$	30.6 ± 0.7	−2.18 ± 0.16	−35.4 ± 0.7	0.115 ±0.004
PEG2k	2000	$(3.3 \pm 1.7) \times 10^6$	2.5 ± 0.2	−9.65 ± 1.24	−37.2 ± 1.6	0.09 ±0.01
PEG3k	3000	$(8.0 \pm 3.0) \times 10^6$	4.8 ± 0.2	−9.3 ± 0.7	−39.4 ± 1.2	0.101 ±0.010
PEG20k	20000	$(1.4 \pm 0.3) \times 10^8$	1.00 ± 0.02	−55.5 ± 1.6	−46.5 ± 0.7	−0.030 ±0.001

[a]Moles of the polymer chain per gram of INTs.

https://doi.org/10.1021/acs.langmuir.1c01549
Langmuir 2021, 37, 9858−9864

The dependence of the affinity toward the Ge−DWINT surface on the PEG molecular weight was further investigated by SANS for PEG2k and PEG20k. It should be noted that the scattering from diluted Ge−DWINT dispersions (1 g·L^{-1}) in the same solvent has a negligible flat scattering intensity in the investigated scattering vector regime (Figure S1). As a general feature (Figure 4), the addition of Ge−DWINTs to PEG

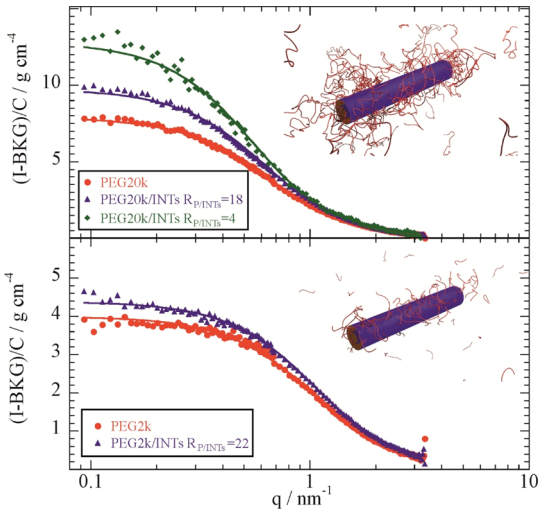

Figure 4. Neutron scattering intensity function after background (BKG) subtraction and polymer concentration normalization (C_P) of PEGs in the presence and absence of Ge−DWINTs (1 g·L^{-1}) at 25 °C. The solvent was H_2O/D_2O with a mass ratio of 1/10. The continuous lines correspond to the fit of the scattering curves (see the text for details).

solutions does not influence the shape of the curves. All scattering curves were analyzed with a model of a Gaussian coil[52]

$$I(q) = I_0 \frac{2[\exp(-q^2 R_g^{\,2}) + q^2 R_g^{\,2} - 1]}{q^4 R_g^{\,4}} \quad (4)$$

with I_0 and R_g being the forward scattering intensity and the radius of gyration of the chain, respectively. The values are given in Table 2. The overlap concentration was calculated from the values of the radii of gyration, as

$$C^* = \frac{Mw}{(4\pi/3) R_g^{\,3} N_A} \quad (5)$$

Confirming that the experiments were performed in the dilute regime, the interactions between the polymer chains can be estimated between the ratio of the determined forward scattering and the predicted value,[53] calculated as

Table 2. Forward Scattering Intensity I_0 and Radius of Gyration R_g Deduced from the Modeling of SANS Curves with a Gaussian Coil Model

system	$R_{P/INTs}$	I_0 exp (cm^{-1})	R_g (nm)	I_0^{calc} (cm^{-1})	I_0 exp / I_0^{calc}
PEG2k		0.08 ± 0.01	1.56 ± 0.08	0.16	0.51
PEG2k/INTs	22	0.10 ± 0.02	1.54 ± 0.05	0.15	0.62
PEG20k		0.18 ± 0.02	2.49 ± 0.06	1.61	0.11
PEG20/INTs	18	0.17 ± 0.02	2.61 ± 0.06	1.22	0.14
	4	0.05 ± 0.01	3.02 ± 0.08	0.30	0.18

$$I_0^{calc} = \frac{\phi_p Mw \Delta\rho^2}{d_p N_A} \quad (6)$$

In eq 6, ϕ_p is the polymer concentration in the volume fraction, d_p is its density (a value of 1.199 g cm^{-3} was used),[54] and $\Delta\rho$ is the scattering contrast. The ratios of 0.5 and 0.1 for PEG2k and PEG20k, respectively, between the experimental and the calculated forward scattering intensity indicate a significant repulsive interaction between the polymer chains, in agreement with previous studies (Table 2).[53]

The analysis of the SANS data shows that the conformation of the polymer is not, or only minimally, affected by the presence of the clay nanotube, as deduced from the constant value of radius of gyration obtained. In contrast, an increase in scattering intensity is observed upon the addition of Ge-DWINTs to the diluted PEG solution. The origin of this increase has to be found in the attractive interaction between the nanoclay and the polymer. In fact, both the adsorption of PEG on the Ge−DWINTs and a reduced repulsion between the PEG chains in solution would result in an increase of the forward scattering intensity. The effect is more pronounced for the longer PEG chains for which the radius of gyration increases from 2.5 to 3 nm with decreasing $R_{P/INTs}$ (Table 2). This slight stretching of PEG20k chains can be ascribed to a crowding phenomenon due to the larger amount of polymers adsorbed onto Ge−DWINTs as predicted by the ITC experiments, *ca.* 0.96 compared to 0.87 for $R_{P/INTs}$ = 4 and 18, respectively. The stretching of the polymer chain is an indication of a relatively compact organization at the solid/liquid interface. This is confirmed by the grafting density of *ca.* 1.6 chains nm^{-2}, estimated from the *Z* values reported in Table 1 and by using the experimental specific volume of Ge−DWINTs (0.3949 cm^3 g^{-1}) and the characteristic sizes of the nanotubes.[14] It should be noted that the fits of the scattering curves for PEG2k provided a radius of gyration of 1.5 nm with and without Ge−DWINTs, in agreement with the thermodynamic prediction of negligible interactions in this case. Therefore, we should expect different rheological and colloidal behaviors for these systems. In particular, depletion processes can play a role for PEG2k/Ge−DWINTs and steric colloidal stabilization for PEG20k/Ge−DWINTs (as a consequence of the large amount of polymers adsorbed onto Ge−DWINT surfaces).

We investigated the flow properties of PEG/Ge−DWINT complexes (PEG2k and PEG20k) prepared at a fixed $R_{P/INTs}$ = 10 while varying the concentration of INTs (C_{INTs}). In this case, the fraction of the polymer adsorbed onto Ge−DWINTs is the same regardless of the value of C_{INTs} but varies by a factor of 2 between the two series (Figure 3). This should allow us to probe how the difference in the amount of PEG adsorbed onto the nanotube surface impacts the viscosity of the suspensions. The flow curves (viscosity η *vs* shear stress σ) exhibit a shear thinning behavior regardless of the molecular weight or the nanotube concentration (Figure 5a,b). With increasing shear stress, hydrodynamic interactions tend to overcome electrostatic interaction between PEG/Ge−DWINT complexes that end up aligning in the flow. To go further, we reproduced flow curves by adjusting a viscosity model based on Quemada's approach[55,56]

https://doi.org/10.1021/acs.langmuir.1c01549
Langmuir 2021, 37, 9858−9864

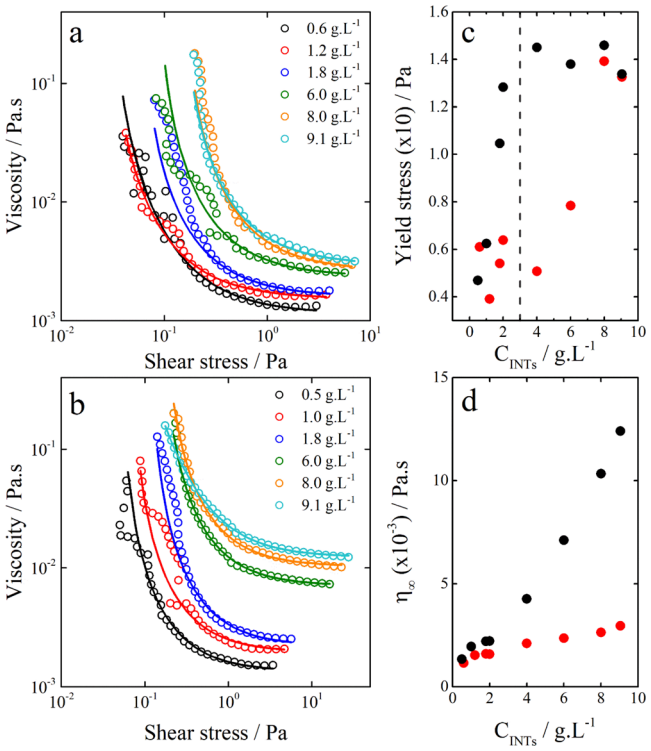

Figure 5. Flow curves for PEG/imogolite mixtures prepared at different C_{INTs} and PEG molecular weights: (a) M_w = 2000 g·mol^{-1} and (b) M_w = 20,000 g·mol^{-1}. Continuous lines correspond to the best fit of eq 7a. The evolution of (c) yield stress and (d) infinite viscosity values with imogolite concentration for PEG2k (red) and PEG20k (black).

$$\eta(\sigma) = \eta_\infty \left(\frac{1 + \sigma/\sigma_c}{\chi + \sigma/\sigma_c} \right)^2 \tag{7a}$$

$$-1 \leq \chi \leq 1 \tag{7b}$$

where η_∞ represents the viscosity for infinite shear stress and σ_c is the critical shear stress. Its value is close to σ when hydrodynamic effects are comparable to Brownian and interaction energies. χ is positive when a viscosity plateau at zero shear is measured, while it is negative when a yield stress σ_y occurs in the dispersion such as $\sigma_y = -\chi\sigma_c$. By adjusting eq 7a using the least-square method, a fair agreement was obtained between the experimental and calculated flow curves for both PEG2k and 20k/Ge−DWINT complexes (Figure 5a,b). The evolution of yield stress σy with Ge−DWINT concentration depending on the PEG molecular weight is represented in Figure 5c. The yield stress remains the same for low Ge−DWINT concentrations but starts to increase when C_{INTs} is above 3 g·L^{-1}.

For the longest PEG chain, we observed a sharp increase of the yield stress right from the first concentrations investigated until reaching a constant value around 0.15 Pa. This difference is directly related to the larger amount of PEG adsorbed on the imogolite surface for PEG20k and the modification of the polymer conformation. This is particularly noticeable when looking at the evolution of infinite shear viscosity (Figure 5d). An almost linear increase is observed with the varying imogolite concentrations, but the values are always lower for PEG2k compared to those for PEG20k. Bridging interactions between the nanotubes seem unlikely since the average distance is at least higher than 60 nm for the most concentrated suspension (~9 g·L^{-1}) that is ~14 times the average diameter of the nanotubes.[24,25] PEG/INT mixtures rather look like a "decorated" nanotube with more or less amounts of the polymer as sketched in Figure 4. For PEG20k, steric interactions between the polymer and the nanotubes may form PEG/Ge−DWINT complexes that are larger than the nanotubes themselves, which interfere more significantly, thus raising the viscosity when shearing.

CONCLUSIONS

In summary, we investigated the adsorption mechanism of nonionic polymers onto geoinspired inorganic nanotubes in aqueous dispersions. Modeling nano-ITC measurements allowed us to quantify the standard variation of enthalpy, entropy, and free energy during the adsorption of PEGs. Their affinity with the nanotube surface is dominated by favorable enthalpic contribution. We also evidenced that the adsorption mechanism depends on the length and molecular weight of the polymer. Within the investigated polymer/Ge−DWINT range, we estimated that more than 95% of the polymer is adsorbed with the longest chain (PEG20k) against 40% for a 10-fold lower polymer molecular weight. The role played by the molecular weight on the adsorption of PEG drastically impacts the high-shear flow properties of the resulting complexes due to the different interactions and conformations of the polymer coil at the interface with the nanotubes. These findings will open a fresh look on the fundamental understanding of polymers with these modeled nanotubes and will also aid in an improved rational design of hybrid polymer/imogolite mixtures during the elaboration of nanocomposites.

ASSOCIATED CONTENT

Supporting Information

The Supporting Information is available free of charge at https://pubs.acs.org/doi/10.1021/acs.langmuir.1c01549.

Details on the ITC data analysis and additional SANS data of Ge−DWINT dispersion (PDF)

AUTHOR INFORMATION

Corresponding Authors

Giuseppe Lazzara − *Department of Physics and Chemistry, University of Palermo, Palermo 90128, Italy*; Phone: +39 09123897962; Email: giuseppe.lazzara@unipa.it

Erwan Paineau − *Université Paris-Saclay, CNRS, Laboratoire de Physique des Solides, Orsay 91405, France*; orcid.org/0000-0002-6776-7201; Phone: +33 (0) 169 156 051; Email: erwan-nicolas.paineau@universite-paris-saclay.fr

Authors

Giuseppe Cavallaro − *Department of Physics and Chemistry, University of Palermo, Palermo 90128, Italy*; orcid.org/0000-0002-2145-0161

Frédéric Pignon − *Laboratoire de Rhéologie et Procédés, Univ. Grenoble Alpes, CNRS, Grenoble INP (Institut of Engineering Univ. Grenoble-Alpes), Grenoble F-38000, France*; orcid.org/0000-0001-5852-3240

Leonardo Chiappisi − *Institut Laue-Langevin, Grenoble 38042, France*

Complete contact information is available at: https://pubs.acs.org/10.1021/acs.langmuir.1c01549

https://doi.org/10.1021/acs.langmuir.1c01549
Langmuir 2021, 37, 9858−9864

Funding

Laboratoire Rhéologie et Procédés is part of LabEx Tec21 (Investissements d'Avenir—grant agreement no. ANR-11-LABX-0030), PolyNat Carnot Institut (Investissements d'Avenir—grant agreement #ANR-16-CARN-0025-01), and Glyco@Alps programme (Investissements d'Avenir—grant agreement #ANR-15-IDEX-02). G.L. and G.C. thank the University of Palermo for the financial support (FFR2020).

Notes

The authors declare no competing financial interest.

■ ACKNOWLEDGMENTS

The present work has benefited from the Imagerie-Gif core facility supported by l'Agence Nationale de la Recherche (ANR-11-EQPX-0029/Morphoscope; ANR-10-INBS-04/FranceBioImaging; and ANR-11-IDEX-0003-02/Saclay Plant Sciences). SANS data (https://doi.ill.fr/10.5291/ILL-DATA.9-12-557) using D11 at Institut Laue Langevin took place with the approved proposal 9-12-557. The Partnership for Soft Condensed Matter (PSCM) is acknowledged for providing the laboratory infrastructure for sample preparation and prechar-acterization.

■ REFERENCES

(1) Dahlgren, R.; Shoji, S.; Nanzyo, M. Mineralogical Characteristics of Volcanic Ash Soils. In *Developments in Soil Science*; Elsevier, 1993; Vol. *21*, pp 101−143. DOI: 10.1016/s0166-2481(08)70266-6

(2) Joussein, E.; Petit, S.; Churchman, J.; Theng, B.; Righi, D.; Delvaux, B. Halloysite Clay Minerals−a Review. *Clay Miner.* **2005**, *40*, 383−426.

(3) Farmer, V. C.; Fraser, A. R.; Tait, J. M. Synthesis of Imogolite - Tubular Aluminum Silicate Polymer. *J. Chem. Soc., Chem. Commun.* **1977**, *13*, 462−463.

(4) Paineau, E. Imogolite Nanotubes: A Flexible Nanoplatform with Multipurpose Applications. *Appl. Sci.* **2018**, *8*, 1921.

(5) Cradwick, P. D. G.; Farmer, V. C.; Russell, J. D.; Masson, C. R.; Wada, K.; Yoshinaga, N. Imogolite, a Hydrated Aluminum Silicate of Tubular Structure. *Nat. Phys. Sci.* **1972**, *240*, 187−189.

(6) Mukherjee, S.; Kim, K.; Nair, S. Short, Highly Ordered, Single-Walled Mixed-Oxide Nanotubes Assemble from Amorphous Nano-particles. *J. Am. Chem. Soc.* **2007**, *129*, 6820−6826.

(7) Thill, A.; Guiose, B.; Bacia-Verloop, M.; Geertsen, V.; Belloni, L. How the Diameter and Structure of (OH)(3)Al2O3SixGe1-XOH Imogolite Nanotubes Are Controlled by an Adhesion versus Curvature Cornpetition. *J. Phys. Chem. C* **2012**, *116*, 26841−26849.

(8) Thill, A.; Maillet, P.; Guiose, B.; Spalla, O.; Belloni, L.; Chaurand, P.; Auffan, M.; Olivi, L.; Rose, J. Physico-Chemical Control over the Single- or Double-Wall Structure of Aluminogermanate Imogolite-like Nanotubes. *J. Am. Chem. Soc.* **2012**, *134*, 3780−3786.

(9) Kang, D.-Y.; Brunelli, N. A.; Yucelen, G. I.; Venkatasubramanian, A.; Zang, J.; Leisen, J.; Hesketh, P. J.; Jones, C. W.; Nair, S. Direct Synthesis of Single-Walled Aminoaluminosilicate Nanotubes with Enhanced Molecular Adsorption Selectivity. *Nat. Commun.* **2014**, *5*, 3342.

(10) Amara, M. S.; Paineau, E.; Rouzière, S.; Guiose, B.; Krapf, M.-E. M.; Taché, O.; Launois, P.; Thill, A. Hybrid, Tunable-Diameter, Metal Oxide Nanotubes for Trapping of Organic Molecules. *Chem. Mater.* **2015**, *27*, 1488−1494.

(11) Picot, P.; Gobeaux, F.; Coradin, T.; Thill, A. Dual Internal Functionalization of Imogolite Nanotubes as Evidenced by Optical Properties of Nile Red. *Appl. Clay Sci.* **2019**, *178*, 105133.

(12) Lisuzzo, L.; Cavallaro, G.; Lazzara, G.; Milioto, S.; Parisi, F.; Stetsyshyn, Y. Stability of Halloysite, Imogolite, and Boron Nitride Nanotubes in Solvent Media. *Appl. Sci.* **2018**, *8*, 1068.

(13) Paineau, E.; Monet, G.; Peyre, V.; Goldmann, C.; Rouzière, S.; Launois, P. Colloidal Stability of Imogolite Nanotube Dispersions: A Phase Diagram Study. *Langmuir* **2019**, *35*, 12451−12459.

(14) Paineau, E.; Rouzière, S.; Monet, G.; Diogo, C. C.; Morfin, I.; Launois, P. Role of Initial Precursors on the Liquid-Crystalline Phase Behavior of Synthetic Aluminogermanate Imogolite Nanotubes. *J. Colloid Interface Sci.* **2020**, *580*, 275−285.

(15) Kang, D.-Y.; Lydon, M. E.; Yucelen, G. I.; Jones, C. W.; Nair, S. Solution-Processed Ultrathin Aluminosilicate Nanotube-Poly(Vinyl Alcohol) Composite Membranes with Partial Alignment of Nano-tubes. *Chemnanomat* **2015**, *1*, 102−108.

(16) Fernandez-Martinez, A.; Tao, J.; Wallace, A. F.; Bourg, I. C.; Johnson, M. R.; De Yoreo, J. J.; Sposito, G.; Cuello, G. J.; Charlet, L. Curvature-Induced Hydrophobicity at Imogolite−water Interfaces. *Environ. Sci.: Nano* **2020**, *7*, 2759−2772.

(17) Nasi, R.; Sannino, F.; Picot, P.; Thill, A.; Oliviero, O.; Esposito, S.; Armandi, M.; Bonelli, B. Hybrid Organic-Inorganic Nanotubes Effectively Adsorb Some Organic Pollutants in Aqueous Phase. *Appl. Clay Sci.* **2020**, *186*, 105449.

(18) Monet, G.; Paineau, E.; Chai, Z.; Amara, M. S.; Orecchini, A.; Jimenéz-Ruiz, M.; Ruiz-Caridad, A.; Fine, L.; Rouzière, S.; Liu, L.-M.; Teobaldi, G.; Rols, S.; Launois, P. Solid Wetting-Layers in Inorganic Nano-Reactors: The Water in Imogolite Nanotube Case. *Nanoscale Adv.* **2020**, *2*, 1869−1877.

(19) Poli, E.; Elliott, J. D.; Ratcliff, L. E.; Andrinopoulos, L.; Dziedzic, J.; Hine, N. D. M.; Mostofi, A. A.; Skylaris, C.-K.; Haynes, P. D.; Teobaldi, G. The Potential of Imogolite Nanotubes as (Co-)Photocatalysts: A Linear-Scaling Density Functional Theory Study. *J. Phys.: Condens. Matter* **2016**, *28*, 074003.

(20) Elliott, J. D.; Poli, E.; Scivetti, I.; Ratcliff, L. E.; Andrinopoulos, L.; Dziedzic, J.; Hine, N. D. M.; Mostofi, A. A.; Skylaris, C.-K.; Haynes, P. D.; Teobaldi, G. Chemically Selective Alternatives to Photoferroelectrics for Polarization-Enhanced Photocatalysis: The Untapped Potential of Hybrid Inorganic Nanotubes. *Adv. Sci.* **2017**, *4*, 1600153.

(21) Olson, N.; Deshpande, N.; Gunduz, S.; Ozkan, U. S.; Brunelli, N. A. Utilizing Imogolite Nanotubes as a Tunable Catalytic Material for the Selective Isomerization of Glucose to Fructose. *Catal. Today* **2019**, *323*, 69−75.

(22) Poli, E.; Elliott, J. D.; Chulkov, S. K.; Watkins, M. B.; Teobaldi, G. The Role of Cation-Vacancies for the Electronic and Optical Properties of Aluminosilicate Imogolite Nanotubes: A Non-Local, Linear-Response TDDFT Study. *Front. Chem.* **2019**, *7*, 210.

(23) Li, J.; Jiménez-Calvo, P.; Paineau, E.; Ghazzal, M. N. Metal Chalcogenides Based Heterojunctions and Novel Nanostructures for Photocatalytic Hydrogen Evolution. *Catalysts* **2020**, *10*, 89.

(24) Paineau, E.; Krapf, M.-E. M.; Amara, M.-S.; Matskova, N. V.; Dozov, I.; Rouzière, S.; Thill, A.; Launois, P.; Davidson, P. A Liquid-Crystalline Hexagonal Columnar Phase in Highly-Dilute Suspensions of Imogolite Nanotubes. *Nat. Commun.* **2016**, *7*, 10271.

(25) Paineau, E.; Launois, P. Influence of the Al/Ge Ratio on the Structure and Self-Organization of Anisometric Imogolite Nanotubes. *Crystals* **2020**, *10*, 1094.

(26) Poli, E.; Elliott, J. D.; Chai, Z.; Teobaldi, G. Termination Effects in Aluminosilicate and Aluminogermanate Imogolite Nano-tubes: A Density Functional Theory Study. *Crystals* **2020**, *10*, 1051.

(27) Park, K.-L.; Ma, W.; Higaki, Y.; Takahara, A. Design and Characterization of Hybrid Hydrogels Composed of Imogolite Fibrous Nanotubular Clay and Hyaluronic Acid. *Polymer* **2016**, *100*, 238−243.

(28) Shikinaka, K. Design of Stimuli-Responsive Materials Consisting of the Rigid Cylindrical Inorganic Polymer "Imogolite. *Polym. J.* **2016**, *48*, 689−696.

(29) Ryu, J.; Ko, J.; Lee, H.; Shin, T.-G.; Sohn, D. Structural Response of Imogolite-Poly(Acrylic Acid) Hydrogel under Deforma-tion. *Macromolecules* **2016**, *49*, 1873−1881.

(30) Su, C.-Y.; Yang, A.-C.; Jiang, J.-S.; Yang, Z.-H.; Huang, Y.-S.; Kang, D.-Y.; Hua, C.-C. Properties of Single-Walled Aluminosilicate

Nanotube/Poly (Vinyl Alcohol) Aqueous Dispersions. *J. Phys. Chem. B* **2018**, *122*, 380−391.
(31) Li, M.; Brant, J. A. Effects of Aluminogermanate Imogolite Nanotube Orientation on Mass Transport across Polyamide Nanocomposite Membranes. *J. Membr. Sci.* **2019**, *585*, 38−51.
(32) Lee, W. J.; Paineau, E.; Anthony, D. B.; Gao, Y.; Leese, H. S.; Rouzière, S.; Launois, P.; Shaffer, M. S. P. Inorganic Nanotube Mesophases Enable Strong Self-Healing Fibers. *ACS Nano* **2020**, *14*, 5570−5580.
(33) Li, L.; Takada, A.; Ma, W.; Fujikawa, S.; Ariyoshi, M.; Igata, K.; Okajima, M.; Kaneko, T.; Takahara, A. Structure and Properties of Hybrid Film Fabricated by Spin-Assisted Layer-by-Layer Assembly of Sacran and Imogolite Nanotubes. *Langmuir* **2020**, *36*, 1718−1726.
(34) Mukai, M.; Takahara, M.; Takada, A.; Takahara, A. Preparation of an (Inorganic/Organic) Hybrid Hydrogel from a Peptide Oligomer and a Tubular Aluminosilicate Nanofiber. *RSC Adv.* **2021**, *11*, 4901−4905.
(35) Bonini, M.; Gabbani, A.; Del Buffa, S.; Ridi, F.; Baglioni, P.; Bordes, R.; Holmberg, K. Adsorption of Amino Acids and Glutamic Acid-Based Surfactants on Imogolite Clays. *Langmuir* **2017**, *33*, 2411−2419.
(36) Kang, D.-Y.; Tong, H. M.; Zang, J.; Choudhury, R. P.; Sholl, D. S.; Beckham, H. W.; Jones, C. W.; Nair, S. Single-Walled Aluminosilicate Nanotube/Poly(Vinyl Alcohol) Nanocomposite Membranes. *ACS Appl. Mater. Interfaces* **2012**, *4*, 965−976.
(37) Lange, T.; Charpentier, T.; Gobeaux, F.; Charton, S.; Testard, F.; Thill, A. Partial Transformation of Imogolite by Decylphosphonic Acid Yields an Interface Active Composite Material. *Langmuir* **2019**, *35*, 4068−4076.
(38) Bertolino, V.; Cavallaro, G.; Lazzara, G.; Milioto, S.; Parisi, F. Biopolymer-Targeted Adsorption onto Halloysite Nanotubes in Aqueous Media. *Langmuir* **2017**, *33*, 3317−3323.
(39) Archer, W. R.; Schulz, M. D. Isothermal Titration Calorimetry: Practical Approaches and Current Applications in Soft Matter. *Soft Matter* **2020**, *16*, 8760−8774.
(40) Cavallaro, G.; Lazzara, G.; Milioto, S. Aqueous Phase/Nanoparticles Interface: Hydroxypropyl Cellulose Adsorption and Desorption Triggered by Temperature and Inorganic Salts. *Soft Matter* **2012**, *8*, 3627−3633.
(41) Holtzer, A.; Holtzer, M. F. Use of the van't Hoff relation in determination of the enthalpy of micelle formation. *J. Phys. Chem.* **1974**, *78*, 1442−1443.
(42) Cavallaro, G.; Donato, D. I.; Lazzara, G.; Milioto, S. Films of Halloysite Nanotubes Sandwiched between Two Layers of Biopolymer: From the Morphology to the Dielectric, Thermal, Transparency, and Wettability Properties. *J. Phys. Chem. C* **2011**, *115*, 20491−20498.
(43) Chiu, C.-W.; Lin, J.-J. Self-Assembly Behavior of Polymer-Assisted Clays. *Prog. Polym. Sci.* **2012**, *37*, 406−444.
(44) El Rifaii, K.; Wensink, H. H.; Bizien, T.; Gabriel, J.-C. P.; Michot, L.; Davidson, P. Destabilization of the Nematic Phase of Clay Nanosheet Suspensions by Polymer Adsorption. *Langmuir* **2020**, *36*, 12563−12571.
(45) Amara, M.-S.; Paineau, E.; Bacia-Verloop, M.; Krapf, M.-E. M.; Davidson, P.; Belloni, L.; Levard, C.; Rose, J.; Launois, P.; Thill, A. Single-Step Formation of Micron Long (OH)3Al2O3Ge(OH) Imogolite-like Nanotubes. *Chem. Commun.* **2013**, *49*, 11284−11286.
(46) Tellinghuisen, J. Calibration in Isothermal Titration Calorimetry: Heat and Cell Volume from Heat of Dilution of NaCl (Aq). *Anal. Biochem.* **2007**, *360*, 47−55.
(47) Lieutenant, K.; Lindner, P.; Gahler, R. A New Design for the Standard Pinhole Small-Angle Neutron Scattering Instrument D11. *J. Appl. Crystallogr.* **2007**, *40*, 1056−1063.
(48) Keiderling, U. The New 'BerSANS-PC'Software for Reduction and Treatment of Small Angle Neutron Scattering Data. *Appl. Phys. A* **2002**, *74*, s1455−s1457.
(49) Breßler, I.; Kohlbrecher, J.; Thünemann, A. F. SASfit: A Tool for Small-Angle Scattering Data Analysis Using a Library of Analytical Expressions. *J. Appl. Crystallogr.* **2015**, *48*, 1587−1598.
(50) Burchill, S.; Hall, P. L.; Harrison, R.; Hayes, M. H. B.; Langford, J. I.; Livingston, W. R.; Smedley, R. J.; Ross, D. K.; Tuck, J. J. Smectite-Polymer Interactions in Aqueous Systems. *Clay Miner.* **1983**, *18*, 373−397.
(51) Luckham, P. F.; Rossi, S. The Colloidal and Rheological Properties of Bentonite Suspensions. *Adv. Colloid Interface Sci.* **1999**, *82*, 43−92.
(52) Debye, P. Molecular-Weight Determination by Light Scattering. *J. Phys. Chem.* **1947**, *51*, 18−32.
(53) Pedersen, J. S.; Sommer, C. Temperature Dependence of the Virial Coefficients and the Chi Parameter in Semi-Dilute Solutions of PEG. *Scattering Methods and the Properties of Polymer Materials*; Springer, 2005, pp 70−78. DOI: 10.1007/b107350
(54) De Lisi, R.; Lazzara, G.; Lombardo, R.; Milioto, S.; Muratore, N.; Liveri, M. L. T. Thermodynamic Behavior of Non-Ionic Tri-Block Copolymers in Water at Three Temperatures. *J. Solut. Chem.* **2006**, *35*, 659−678.
(55) Baravian, C.; Vantelon, D.; Thomas, F. Rheological Determination of Interaction Potential Energy for Aqueous Clay Suspensions. *Langmuir* **2003**, *19*, 8109−8114.
(56) Paineau, E.; Michot, L. J.; Bihannic, I.; Baravian, C. Aqueous Suspensions of Natural Swelling Clay Minerals. 2. Rheological Characterization. *Langmuir* **2011**, *27*, 7806−7819.

https://doi.org/10.1021/acs.langmuir.1c01549
Langmuir 2021, 37, 9858−9864